Title
Reconnection-driven Particle Acceleration in Relativistic Shear Flows

Journal
The Astrophysical Journal Letters, 907(2)

ISSN
2041-8205

Authors
Sironi, Lorenzo
Rowan, Michael E
Narayan, Ramesh

Publication Date
2021-02-01

DOI
10.3847/2041-8213/abd9bc

Peer reviewed

Reconnection-driven Particle Acceleration in Relativistic Shear Flows

Lorenzo Sironi[1], Michael E. Rowan[2], and Ramesh Narayan[3]

[1] Department of Astronomy and Columbia Astrophysics Laboratory, Columbia University, New York, NY 10027, USA; lsironi@astro.columbia.edu
[2] Lawrence Berkeley National Laboratory, Berkeley, CA 94720, USA; mrowan@lbl.gov
[3] Harvard-Smithsonian Center for Astrophysics, Cambridge, MA 02138, USA; rnarayan@cfa.harvard.edu

Abstract

Particle energization in shear flows is invoked to explain nonthermal emission from the boundaries of relativistic astrophysical jets. Yet the physics of particle injection, i.e., the mechanism that allows thermal particles to participate in shear-driven acceleration, remains unknown. With particle-in-cell simulations, we study the development of Kelvin–Helmholtz (KH) instabilities seeded by the velocity shear between a relativistic magnetically dominated electron–positron jet and a weakly magnetized electron–ion ambient plasma. We show that, in their nonlinear stages, KH vortices generate kinetic-scale reconnection layers, which efficiently energize the jet particles, thus providing a first-principles mechanism for particle injection into shear-driven acceleration. Our work lends support to spine-sheath models of jet emission—with a fast core/spine surrounded by a slower sheath—and can explain the origin of radio-emitting electrons at the boundaries of relativistic jets.

1. Introduction

Shear flows are ubiquitous in space and astrophysical plasmas. The free energy of the velocity shear is invoked to accelerate charged particles to nonthermal energies (Rieger 2019)—via a mechanism akin to the Fermi process in converging flows (Fermi 1949). Shear-driven acceleration relies on particles scattering in between regions that move toward each other because of the velocity shear. This requires the mean free path to be sufficiently long to sample a significant velocity gradient. In fact, the major unknown of shear-driven acceleration models is the "injection stage," i.e., the mechanism(s) to promote thermal particles—that cannot participate in shear acceleration, due to their short mean free path—to nonthermal energies.

Shear layers may be prone to the Kelvin–Helmholtz instability (KHI). The KHI has been thoroughly studied with linear stability analysis (Blumen et al. 1975; Ferrari et al. 1978, 1980; Sharma & Chhajlani 1998; Komissarov 1999; Bodo et al. 2004; Osmanov et al. 2008; Prajapati & Chhajlani 2010; Sobacchi & Lyubarsky 2018; Berlok & Pfrommer 2019) and fluid-type simulations, including relativistic effects and magnetic fields (Keppens et al. 1999; Ryu et al. 2000; Zhang et al. 2009; Hamlin & Newman 2013; Millas et al. 2017). In shear layers with flow-aligned magnetic fields, KH vortices can wrap up the field lines onto themselves, leading to dissipation via reconnection (Faganello et al. 2008a, 2010, 2012; Nakamura & Fujimoto 2008; Henri et al. 2013; Nakamura et al. 2013; Nakamura & Daughton 2014; Fadanelli et al. 2018; see also Tolman et al. 2018, for reconnection in KHI-stable shear flows).

In this Letter, we employ fully kinetic particle-in-cell (PIC) simulations to demonstrate that particles are efficiently accelerated at reconnecting current sheets generated self-consistently by the KHI nonlinear stages (Faganello et al. 2008a, 2012). Our study is motivated by the limb-brightened appearance of relativistic jets, e.g., in Cygnus A (Boccardi et al. 2016) and M87 (Walker et al. 2018). Instabilities at relativistic jet boundaries are seen in general-relativistic magnetohydrodynamic (MHD) simulations (Chatterjee et al. 2019), which, however, cannot probe the particle acceleration physics. Our work provides a first-principles mechanism for particle injection into shear-driven acceleration in relativistic magnetically dominated jets. This lends support to spine-sheath models of jet emission (Sikora et al. 2016) and can explain the origin of radio-emitting electrons at the boundaries of relativistic jets.

2. Numerical Method and Setup

We perform ab initio PIC simulations with TRISTAN-MP (Buneman 1993; Spitkovsky 2005). We conduct two-dimensional (2D) simulations in the xy plane, retaining all three components of velocities and electromagnetic fields. The fluid bulk motion is initialized along y, with velocity gradient along x. The domain has length L_y along y ($0 \leqslant y/L_y \leqslant 1$), and width $L_x = 3L_y$ along x ($-1.5 \leqslant x/L_y \leqslant 1.5$), with double-periodic boundaries. We initialize a relativistic magnetically dominated jet at $|x|/L_x \lesssim 0.25$, and a weakly magnetized stationary ambient plasma at $|x|/L_x \gtrsim 0.25$ (which we call "wind," since it should represent the wind of the accretion flow). The simulation is performed in the wind frame.

The jet is composed of cold electron–positron pairs with comoving density n_0—we employ four particles per cell, including both species—and moves with four-velocity $\Gamma_0\beta_0 = 1.3$ along $+\hat{y}$ (we also investigate $\Gamma_0\beta_0 = 3$ and 10). It carries an energetically dominant magnetic field, whose in-plane strength $B_{\mathrm{j},y}$ is parameterized by the magnetization $\sigma_{\mathrm{j},y} = B_{\mathrm{j},y}^2/(4\pi n_0 m_{\mathrm{e}} c^2)$. We also initialize an out-of-plane field $B_{\mathrm{j},z} = B_{\mathrm{j},y}\tan\theta$ and its associated motional electric field $E_{\mathrm{j},x} = -\beta_0 B_{\mathrm{j},z}$. Our reference runs employ $\sigma_{\mathrm{j},y} = 6.7$ and $\theta = 75°$ (corresponding to $\theta' = 65°$ in the jet frame for $\Gamma_0\beta_0 = 1.3$), since astrophysical jets are magnetically dominated and have comparable poloidal (here, along y) and toroidal (along z) jet-frame fields (see Liang et al. 2013a, 2013b; Alves et al. 2014, 2015; Nishikawa et al. 2014, 2016; Pausch et al. 2017 for PIC studies of KHI in unmagnetized plasmas).

The wind is composed of an electron–ion plasma with density $n_{\mathrm{w}} = 128\, n_0$. We typically employ a mass ratio $m_{\mathrm{i}}/m_{\mathrm{e}} = 25$, but we have tested that the late-time particle spectrum is the same for $m_{\mathrm{i}}/m_{\mathrm{e}} = 5$, 25, 100, and also for the artificial case $m_{\mathrm{i}}/m_{\mathrm{e}} = 1$. As we show below, particle energization primarily involves the jet

particles, and so our results are insensitive to the mass ratio in the wind. The wind is initialized with an out-of-plane field $B_{w,z} = 0.1\,B_{j,z}$. The wind plasma beta $\beta_p \approx [B_{j,y}^2 + (\Gamma_0^{-1}B_{j,z})^2]/B_{w,z}^2 \approx 40 \gg 1$, so the wind is particle-dominated (we obtained similar results with stronger $B_{w,z}$, giving $\beta_p \approx$ few).

Our unit of length is the skin-depth of jet particles, $c/\omega_p = \sqrt{m_e c^2/(4\pi e^2 n_0)}$, which we resolve with 11.3 cells. Our reference runs have $L_y = L_0 \equiv 3840$ cells $\approx 340\,c/\omega_p$, but we also present larger runs with $L_y = 3L_0 \approx 1020\,c/\omega_p$ to demonstrate that we achieve asymptotically converged results. In our reference run, the code conserves energy within 0.5%.

The wind and jet properties are smoothly connected with spatial profiles varying as $\tanh[2\pi(x - x_{SL})/\Delta]$ near the shear layers at $|x| = x_{SL} \approx 0.25\,L_x$. We employ wide shear layers with $\Delta \gg c/\omega_p$, in application to realistic jet/wind boundaries. We typically employ $\Delta = 64\,c/\omega_p$, but we report identical results obtained with $\Delta = 192\,c/\omega_p$. For $\Delta \gg c/\omega_p$, the KHI growth should be independent of kinetic physics, and in fact our measured growth rates are in good agreement with MHD expectations (Bodo et al. 2004). The spatial profiles of temperature, charge density, and electric current density follow from pressure equilibrium and Maxwell's equations.

3. Results

The temporal evolution of the KHI is presented in Figure 1, where color indicates the out-of-plane field B_z, with in-plane field lines overlaid. The instability develops in two stages: a mode with wavelength $\lambda \approx L_y/2$ appears in (b), whereas a longer-wavelength mode with $\lambda \approx L_y$ grows at later times. The corresponding growth rates are in good agreement with MHD linear dispersion analysis. The vortices created by the nonlinear stages of the KHI bend the in-plane field lines, creating antiparallel configurations prone to reconnection (d) and plasmoid formation, see the Appendix. The final stage (e) is characterized by (i) the persistence of a nearly unperturbed jet core (yellow) surrounded by a sheath of weaker B_z (red), whose width is $\approx 0.3\,L_y$; and (ii) the presence of magnetized "clouds" of jet material—on a variety of scales, from plasma scales up to $\approx 0.3\,L_y$—in pressure equilibrium with the surrounding wind plasma.

The evolution of the KHI is further analyzed in Figure 2. The jet starts with bulk four-velocity $\Gamma\beta_y = \Gamma_0\beta_0 = 1.3$ (blue in (a)), and it is magnetically dominated, with $\sigma_y \approx \sigma_{j,y} = 6.7$ (dotted blue in (b)) and $\sigma_z = \sigma_y \tan^2\theta \approx 93.3$ ($\sigma_i \equiv B_i^2/4\pi n_0 m_e c^2$ is the magnetization contributed by B_i). When the KHI grows nonlinear, the in-plane field lines are twisted and folded, and a significant B_x develops at the jet boundaries, with peak $\sigma_x \approx 4$ (green and yellow in (b)). Since part of the magnetic energy will be dissipated by reconnection, the peak value of σ_x can be a proxy for the characteristic magnetization of reconnecting current sheets. Since $\sigma_x \gtrsim 1$, KHI-driven reconnection occurs in the relativistic regime.

The end stage (red lines) shows a velocity profile characterized by a fast jet core ($|x| \lesssim 100\,c/\omega_p$), moving nearly at the initial speed, surrounded by wings (or, a sheath) of slower-moving material ($100 \lesssim |x| \lesssim 250\,c/\omega_p$), with $\Gamma\beta_y \approx 0.5$. A trans-relativistic sheath also characterizes the final stages of simulations with faster jets ($\Gamma_0\beta_0 = 3$ and $\Gamma_0\beta_0 = 10$). In the sheath near $|x| \approx 200\,c/\omega_p$, the in-plane magnetic energy density (dotted red in (b)) is nearly in equipartition with the electron energy density (solid red in (c)), or equivalently, the plasma beta $\beta_p \approx 1$. This is a generic outcome of relativistic reconnection (Sironi et al. 2016).

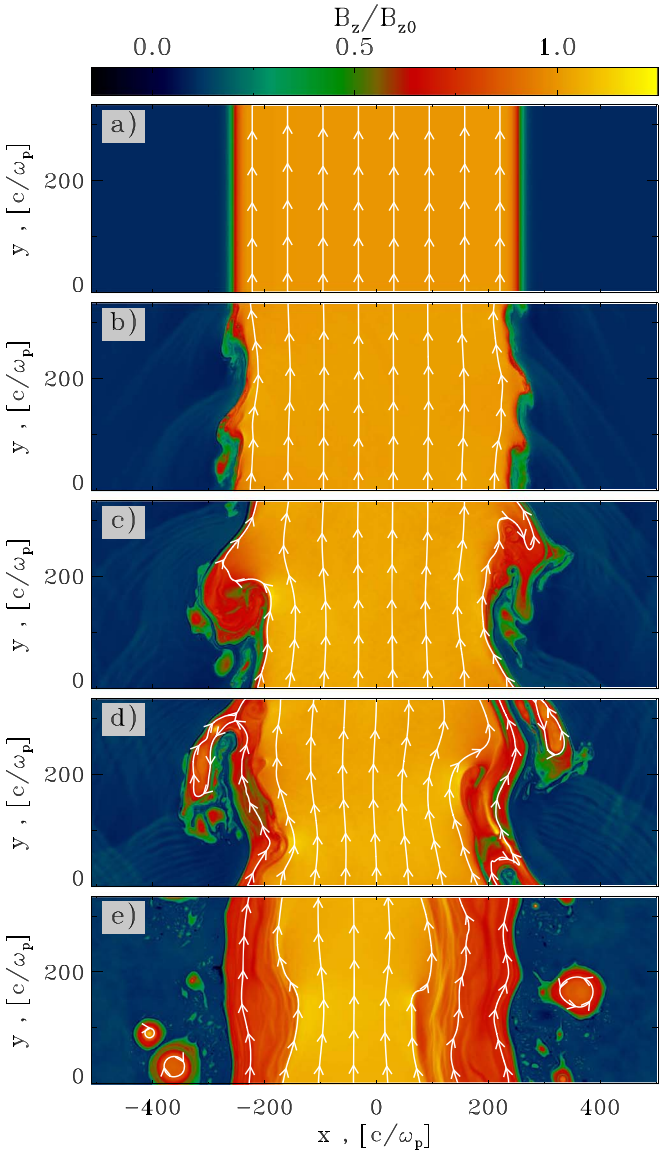

Figure 1. 2D evolution of the out-of-plane field B_z (color)—in units of the initial jet field $B_{z0} \equiv B_{j,z}$—at (a) $\omega_p t = 80$, (b) $\omega_p t = 3262$, (c) $\omega_p t = 4216$, (d) $\omega_p t = 5171$, and (e) $\omega_p t = 12569$, with in-plane field lines overlaid. The jet is initially at $|x| \lesssim 250\,c/\omega_p$, surrounded by the wind.

The nonlinear development of the KHI leads to efficient particle acceleration (top panel of Figure 3). Initially, wind electrons populate a nonrelativistic Maxwellian (dashed lines), while the spectrum of jet electrons peaks at their bulk energy $\Gamma_0 - 1 \approx 0.7$ (solid blue). Concurrently with the formation of KHI-induced current sheets, a distinct high-energy component emerges, primarily populated by jet particles (green and yellow correspond to Figures 1(c) and (d)). The spectral cutoff shifts up at every stage of nonlinear KHI development (i.e., first with the $\lambda \approx L_y/2$ mode going nonlinear, and then with the $\lambda \approx L_y$ mode). In the final stage (red lines), the spectrum extends up to a cutoff energy $\gamma_e - 1 \approx 30$, as expected from reconnection-driven particle acceleration if the in-plane magnetization ≈ 10 (Werner et al. 2016; Petropoulou & Sironi 2018), as inferred from Figure 2(b). The electron spectrum at even later times (not shown) is nearly identical to the red curve, i.e., the system has reached a steady state, with $\sim 60\%$ of the dissipated magnetic energy transferred to $\gamma_e > 3$ jet particles. At all times, the

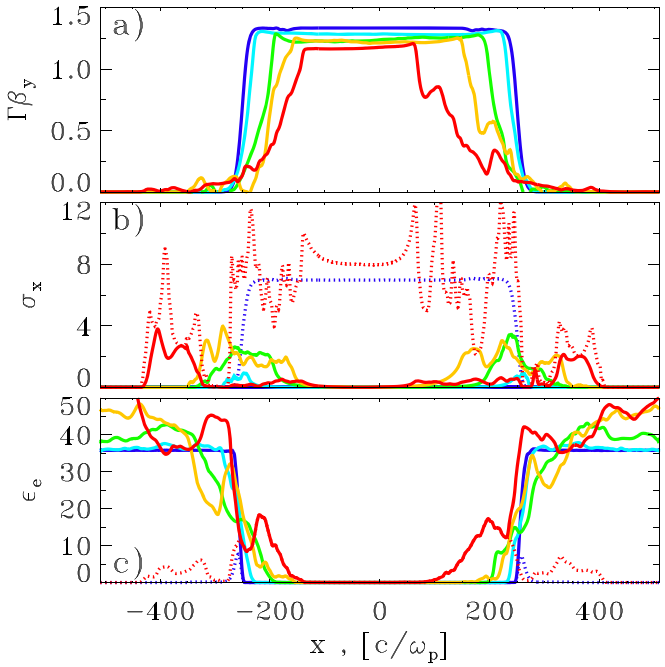

Figure 2. Temporal evolution of y-averaged profiles, with colors from blue to red referring to the same times as panels in Figure 1. (a) Bulk four-velocity along y, in units of c, where in each cell the fluid speed is computed by averaging over velocities of individual particles. (b) Local magnetization from B_x (solid lines), i.e., $\sigma_x = B_x^2/(4\pi n_0 m_e c^2)$. Dotted lines represent the magnetization $\sigma_x+\sigma_y$ from in-plane fields, at the initial (blue) and final (red) times. (c) Total electron internal energy density normalized to the initial rest-mass energy density of jet electrons. Dotted lines refer to jet electrons only, at the initial (blue) and final (red) times.

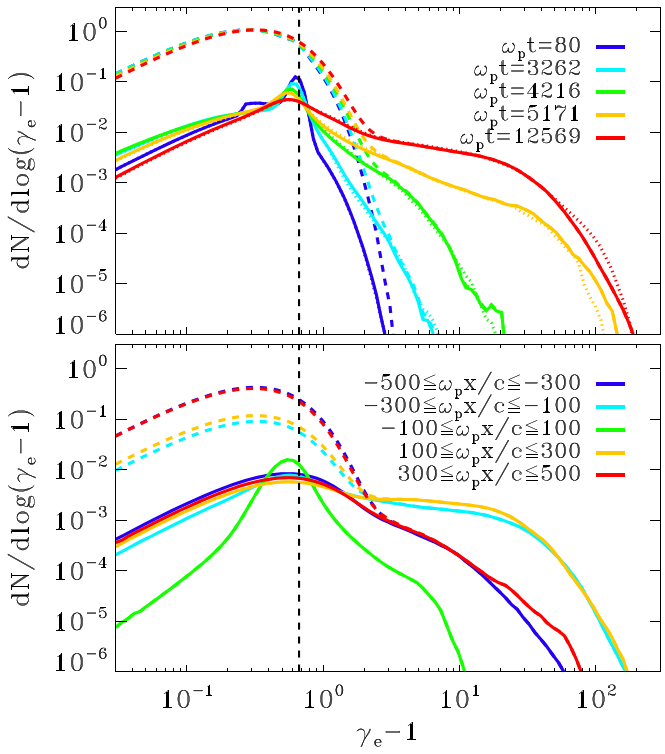

Figure 3. Top: temporal evolution of the electron spectrum (the times in the legend correspond to panels in Figure 1), for all electrons (dashed), jet electrons (solid), and jet positrons (dotted). Bottom: at the final time $\omega_p t = 12569$, spatial dependence of the electron spectrum (see legend), for all electrons (dashed) and jet electrons (solid). The vertical black dashed line is at the bulk energy $\Gamma_0 - 1$.

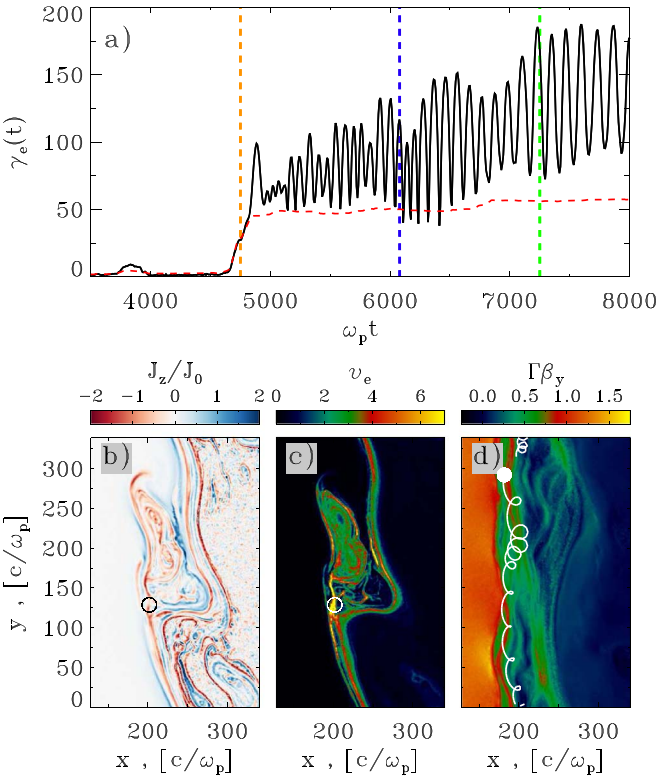

Figure 4. Trajectory of a representative high-energy electron. Panel (a): time evolution of Lorentz factor (solid black line) and parallel work $W_\parallel = -e\int_0^t E_\parallel v_\parallel dt' / m_e c^2$ (dashed red line), where $E_\parallel = \boldsymbol{E}\cdot\hat{\boldsymbol{b}}$ and $v_\parallel = \boldsymbol{v}\cdot\hat{\boldsymbol{b}}$ (here, $\boldsymbol{E}$ is the electric field, $\boldsymbol{v}$ the electron velocity, and $\hat{\boldsymbol{b}} = \boldsymbol{B}/B$ the magnetic field unit vector). Panels (b) and (c): 2D structure of the out-of-plane current J_z (in units of $J_0 = en_0c$) and of the mean internal energy per electron υ_e (in units of $m_e c^2$), at the time $\omega_p t = 4750$ of particle injection (vertical dashed orange line in (a)). The electron position is indicated by the circle. Panel (d): 2D structure of the bulk four-velocity along y, in units of c, at $\omega_p t \approx 7250$ (vertical dashed green line in (a)). The electron position at this time is indicated by the filled circle, and we also plot its trajectory from $\omega_p t = 6080$ (blue dashed line in (a)) to $\omega_p t = 7250$ (green dashed line in (a)).

spectrum of jet positrons (dotted) is nearly identical to that of jet electrons (solid).

Most of the accelerated electrons and positrons are localized at jet boundaries, with nearly identical outcomes from the left and right sides (bottom panel in Figure 3, cyan and yellow). The jet core (green) retains a narrow spectrum centered at $\Gamma_0 - 1 \approx 0.7$. The high-energy particles at $|x| \gtrsim 300\, c/\omega_p$ (blue and red lines) were initially in the jet, and now they reside in the magnetized clouds embedded in the wind (Figure 1(e)).

The trajectory of a representative high-energy electron is displayed in Figure 4. The first stage of acceleration ($\omega_p t \approx 4750$, vertical orange in (a)) is powered by $E_\parallel = \boldsymbol{E}\cdot\hat{\boldsymbol{b}}$ (compare solid black and red dashed lines). The dominance of the nonideal electric field $E_\parallel$ in the process of particle acceleration is expected for reconnection-powered acceleration with a strong nonalternating component (Ball et al. 2019; Comisso & Sironi 2019), although other mechanisms may also play a role (Guo et al. 2019). During this injection stage, the electron is located within a reconnecting current sheet (b), where particle acceleration/heating occurs (c). At later times, while $E_\parallel$ no longer contributes to acceleration, the electron energy still steadily grows—a similar two-stage acceleration process was reported for magnetically dominated plasma turbulence (Comisso & Sironi 2018, 2019). In this time range (between vertical dashed blue and green in (a)), the

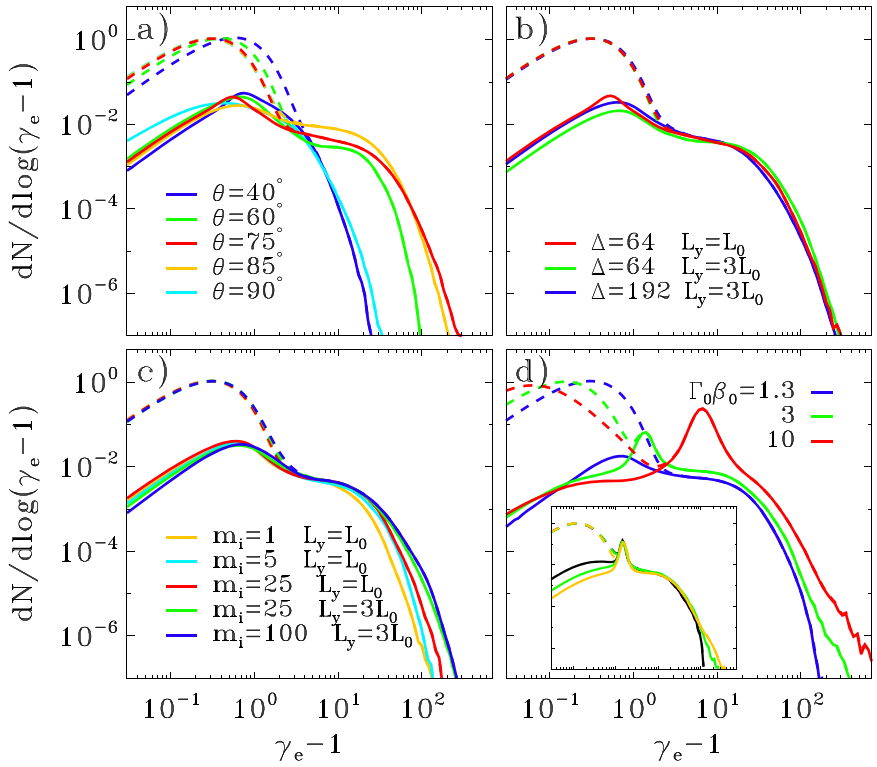

Figure 5. Dependence of the late-time electron spectrum (measured at $t \approx 31\, L_y/c$) on physical parameters, for all electrons (dashed) and jet electrons (solid). Unless otherwise noted, we employ numerical and physical parameters as in our reference run. We vary: (a) The angle $\theta = \arctan(B_{j,z}/B_{j,y})$, keeping the initial $B_{j,y}^2 + B_{j,z}^2$ fixed. (b) The layer width Δ (in units of c/ω_p) and the box size L_y. (c) The ion mass m_i (in units of m_e). Yellow, cyan, and red refer to our reference box, while green and blue to a box with wider $\Delta = 192\, c/\omega_p$ and larger $L_y = 3L_0$. (d) The jet bulk four-velocity, in simulations with $m_i/m_e = 1$ and $\Delta = 16\, c/\omega_p$. Inset: box-size dependence for $\Gamma_0\beta_0 = 3$, with the reference box (green), and a box twice smaller (black) and larger (orange).

electron gains energy while moving back and forth across the shear layer (d), as expected in shear-driven acceleration. The electron orbit covers a sizeable fraction of the shear-layer width, and so it can experience a significant velocity gradient.

To assess the generality of reconnection-powered injection in KHI-unstable shear layers, in Figure 5 we present the dependence of the spectrum of all electrons (dashed) and jet electrons (solid) on several physical parameters. Spectra are shown at sufficiently late times that the system is in steady state. When varying $\theta = \arctan(B_{j,z}/B_{j,y})$ at fixed $B_{j,y}^2 + B_{j,z}^2$ (Figure 5(a)), we find that reconnection-driven particle acceleration is most efficient at intermediate angles, $60° \lesssim \theta \lesssim 85°$. At smaller angles ($\theta = 40°$), the shear layer is KHI-stable. In the absence of in-plane fields ($\theta = 90°$), reconnection cannot operate, and we report only marginal evidence for accelerated particles, with cutoff energy much smaller than in our reference run (see also Cerutti & Giacinti 2020). The high-energy spectral cutoff does not significantly vary for $60° \lesssim \theta \lesssim 85°$, which follows from the weak dependence on θ of the typical magnetization of KHI-generated current sheets (as tracked by the peak σ_x). In turn, this is due to a combination of two opposite effects: at larger θ, the initial $\sigma_{j,y}$ is smaller, yet the KHI is more effective in folding the field lines (precisely because of the weaker tension of in-plane fields), which results, overall, in comparable magnetizations of the self-generated current sheets. Given that black hole jets start with predominantly poloidal fields (here, along y), while they are dominated by toroidal fields (here, along z) at large distances, our results in Figure 5(a) may help put constraints on the distance where KHI-driven reconnection and ensuing particle acceleration is most effective.

We demonstrate in Figure 5(b) that our results hold in the MHD limit L_y, $\Delta \gg c/\omega_p$. Also, electron spectra show only a weak dependence on the ion-to-electron mass ratio in the wind (c); this is expected, given that acceleration mostly involves electrons and positrons in the jet.

Figure 5(d) illustrates the dependence on the initial jet velocity: with increasing $\Gamma_0\beta_0$, a separate population emerges at high energies ($\gamma_e \gtrsim 200$), beyond the bump of reconnection-accelerated particles at $\gamma_e \lesssim 100$. By tracking the trajectories of the highest-energy electrons reaching $\gamma_e \gtrsim 200$, we find that they are accelerated first by reconnection, and then by scattering back and forth across the shear layer (as in Figure 4), i.e., they participate in shear-driven acceleration. In larger domains, the maximum energy of shear-accelerated particles increases (inset in Figure 5(d)).

4. Conclusions

By means of large-scale 2D PIC simulations, we study the physics of particle acceleration in KHI-unstable shear layers, for the conditions expected at boundaries of relativistic magnetically dominated jets. We start from shear layers much wider than kinetic scales. We find that the nonlinear evolution of KH vortices leads to reconnection of the jet field, which results in efficient acceleration of jet electrons and positrons. The highest-energy particles resulting from reconnection are further energized by shear-driven acceleration, i.e., reconnection can mediate particle injection into shear acceleration. Our work lends support to spine-sheath models of jet emission and can explain the origin of radio-emitting electrons at the boundaries of relativistic jets (see Ripperda et al. 2020 for an alternative explanation).

We defer an investigation of 3D effects to future work, though we note that simulations of relativistic reconnection

(Guo et al. 2014; Sironi & Spitkovsky 2014; Werner & Uzdensky 2017; Sironi & Beloborodov 2020) and magnetically dominated plasma turbulence (Comisso & Sironi 2018, 2019) yield similar results between 2D and 3D. We also leave to future work a more detailed characterization of the properties of shear-accelerated particles (e.g., acceleration efficiency, power-law slope, scattering, and acceleration rates).

This work is supported in part by NASA via the TCAN award grant NNX14AB47G and by the black hole initiative at Harvard University, which is supported by a grant from the Templeton Foundation. L.S. acknowledges support from the Sloan Fellow-ship, the Cottrell Scholar Award, NASA ATP NNX17AG21G, NSF PHY-1903412, and DoE DE-SC0021254. The simulations have been performed at Columbia (Habanero and Terremoto), and with NASA (Pleiades) resources.

Appendix
KHI-driven Reconnection Plasmoids

Studies focusing on the Earth magnetosphere have emphasized that the evolution of the KHI can result in vortex-induced magnetic reconnection (Faganello et al. 2008a, 2010, 2012; Nakamura & Fujimoto 2008; Henri et al. 2013; Nakamura et al. 2013; Nakamura & Daughton 2014; Fadanelli et al. 2018) and vortex-induced Rayleigh–Taylor instability (Matsumoto & Hoshino 2004; Faganello et al. 2008b). In the main body of the paper we have demonstrated that, in the case of relativistic jet boundaries, the nonlinear development of the KHI naturally produces reconnection current sheets, which are conducive to efficient particle acceleration. Long reconnection layers are known to be prone to the tearing mode instability (Uzdensky et al. 2010; Huang & Bhattacharjee 2012; Loureiro et al. 2012), which breaks the current sheet into a chain of plasmoids/flux ropes. In Figure 6, we show that this indeed occurs for KHI-generated reconnection layers: the KH vortex in the upper half of the left panel displays two reconnection plasmoids (marked by the arrows in the zoom-in view on the right panel). We argue that reconnection plasmoids, together with nonlinear structures generated by the KHI, can provide the scattering required for shear-driven acceleration.

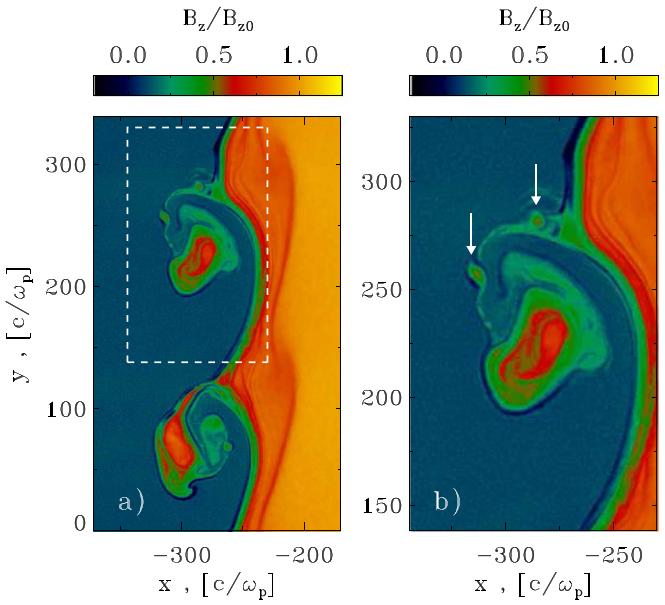

Figure 6. 2D structure of the out-of-plane field B_z, in units of $B_{z0} \equiv B_{j,z}$, from a simulation with $\theta = 60°$, whose late-time spectrum is shown by the green line in Figure 5(a). Both panels refer to $\omega_p t = 3740$, when the $\lambda \approx L_y/2$ mode goes nonlinear. The right panel is a zoom-in view of the left panel (from the area delimited by the white dashed lines), and it shows the presence of two reconnection plasmoids (as marked by the white arrows).

ORCID iDs

Lorenzo Sironi https://orcid.org/0000-0002-1227-2754
Michael E. Rowan https://orcid.org/0000-0003-2406-1273

References

Alves, E. P., Grismayer, T., Fonseca, R. A., & Silva, L. O. 2014, NJPh, 16, 035007
Alves, E. P., Grismayer, T., Fonseca, R. A., & Silva, L. O. 2015, PhRvE, 92, 021101
Ball, D., Sironi, L., & Özel, F. 2019, ApJ, 884, 57
Berlok, T., & Pfrommer, C. 2019, MNRAS, 485, 908
Blumen, W., Drazin, P. G., & Billings, D. F. 1975, JFM, 71, 305
Boccardi, B., Krichbaum, T. P., Bach, U., et al. 2016, A&A, 585, A33
Bodo, G., Mignone, A., & Rosner, R. 2004, PhRvE, 70, 036304
Buneman, O. 1993, Computer Space Plasma Physics (Tokyo: Terra Scientific), 67
Cerutti, B., & Giacinti, G. 2020, A&A, 642, A123
Chatterjee, K., Liska, M., Tchekhovskoy, A., & Markoff, S. B. 2019, MNRAS, 490, 2200
Comisso, L., & Sironi, L. 2018, PhRvL, 121, 255101
Comisso, L., & Sironi, L. 2019, ApJ, 886, 122
Fadanelli, S., Faganello, M., Califano, F., et al. 2018, JGRA, 123, 9340
Faganello, M., Califano, F., & Pegoraro, F. 2008a, PhRvL, 101, 105001
Faganello, M., Califano, F., & Pegoraro, F. 2008b, PhRvL, 100, 015001
Faganello, M., Califano, F., Pegoraro, F., Andreussi, T., & Benkadda, S. 2012, PPCF, 54, 124037
Faganello, M., Pegoraro, F., Califano, F., & Marradi, L. 2010, PhPl, 17, 062102
Fermi, E. 1949, PhRv, 75, 1169
Ferrari, A., Trussoni, E., & Zaninetti, L. 1978, A&A, 64, 43
Ferrari, A., Trussoni, E., & Zaninetti, L. 1980, MNRAS, 193, 469
Guo, F., Li, H., Daughton, W., & Liu, Y.-H. 2014, PhRvL, 113, 155005
Guo, F., Li, X., Daughton, W., et al. 2019, ApJL, 879, L23
Hamlin, N., & Newman, W. 2013, PhRvE, 87, 043101
Henri, P., Cerri, S. S., Califano, F., et al. 2013, PhPl, 20, 102118
Huang, Y.-M., & Bhattacharjee, A. 2012, PhRvL, 109, 265002
Keppens, R., Tóth, G., Westermann, R., & Goedbloed, J. 1999, JPlPh, 61, 1
Komissarov, S. S. 1999, MNRAS, 303, 343
Liang, E., Boettcher, M., & Smith, I. 2013a, ApJL, 766, L19
Liang, E., Fu, W., Boettcher, M., Smith, I., & Roustazadeh, P. 2013b, ApJL, 779, L27
Loureiro, N. F., Samtaney, R., Schekochihin, A. A., & Uzdensky, D. A. 2012, PhPl, 19, 042303
Matsumoto, Y., & Hoshino, M. 2004, GeoRL, 31, L02807
Millas, D., Keppens, R., & Meliani, Z. 2017, MNRAS, 470, 592
Nakamura, T. K. M., & Daughton, W. 2014, GeoRL, 41, 8704
Nakamura, T. K. M., Daughton, W., Karimabadi, H., & Eriksson, S. 2013, JGRA, 118, 5742
Nakamura, T. K. M., & Fujimoto, M. 2008, PhRvL, 101, 165002
Nishikawa, K. I., Frederiksen, J. T., Nordlund, Å., et al. 2016, ApJ, 820, 94
Nishikawa, K. I., Hardee, P. E., Duţan, I., et al. 2014, ApJ, 793, 60
Osmanov, Z., Mignone, A., Massaglia, S., Bodo, G., & Ferrari, A. 2008, A&A, 490, 493
Pausch, R., Bussmann, M., Huebl, A., et al. 2017, PhRvE, 96, 013316
Petropoulou, M., & Sironi, L. 2018, MNRAS, 481, 5687
Prajapati, R. P., & Chhajlani, R. K. 2010, PhPl, 17, 112108
Rieger, F. M. 2019, Galax, 7, 78
Ripperda, B., Bacchini, F., & Philippov, A. A. 2020, ApJ, 900, 100
Ryu, D., Jones, T. W., & Frank, A. 2000, ApJ, 545, 475
Sharma, P. K., & Chhajlani, R. K. 1998, PhPl, 5, 625
Sikora, M., Rutkowski, M., & Begelman, M. C. 2016, MNRAS, 457, 1352
Sironi, L., & Beloborodov, A. M. 2020, ApJ, 899, 52
Sironi, L., Giannios, D., & Petropoulou, M. 2016, MNRAS, 462, 48
Sironi, L., & Spitkovsky, A. 2014, ApJL, 783, L21
Sobacchi, E., & Lyubarsky, Y. E. 2018, MNRAS, 473, 2813

Spitkovsky, A. 2005, in AIP Conf. Ser. 801, Astrophysical Sources of High Energy Particles and Radiation, ed. T. Bulik, B. Rudak, & G. Madejski (Melville, NY: AIP), 345
Tolman, E. A., Loureiro, N. F., & Uzdensky, D. A. 2018, JPlPh, 84, 905840115
Uzdensky, D. A., Loureiro, N. F., & Schekochihin, A. A. 2010, PhRvL, 105, 235002
Walker, R. C., Hardee, P. E., Davies, F. B., Ly, C., & Junor, W. 2018, ApJ, 855, 128
Werner, G. R., & Uzdensky, D. A. 2017, ApJL, 843, L27
Werner, G. R., Uzdensky, D. A., Cerutti, B., Nalewajko, K., & Begelman, M. C. 2016, ApJL, 816, L8
Zhang, W., MacFadyen, A., & Wang, P. 2009, ApJL, 692, L40